Journal of Computational Applied Mechanics 2026, 57(3): 538-553

DOI: 10.22059/jcamech.2026.416706.1852

RESEARCH PAPER

Double-Diffusive Heat and Mass Transfer in Unsteady MHD Casson Nanofluid Flow over a Bidirectional Stretching Surface with Cattaneo–Christov Heat Flux

Ji-Huan He [a, *], M. Y Adamu [b], Isah Abdullahi [a, b,†]

[a] *School of Information Engineering, Yango University, Fuzhou 350015, China.*
[b] *Abubakar Tafawa Balewa University, Bauchi, Nigeria.*

Abstract

This work presents a theoretical investigation on unsteady magnetohydrodynamic (MHD) boundary layer flow of Casson nanofluids over a bidirectional stretching surface, with an emphasis on double-diffusive heat and mass transfer. To overcome the limitation of classical Fourier's law, the Cattaneo–Christov heat flux model is employed to consider thermal relaxation time and finite heat propagation velocity. The mathematical model fully couples multiple physical mechanisms including thermal radiation, viscous dissipation, porous medium effect, Brownian motion and thermophoresis. Based on similarity transformations, the partial differential equations governing mass, momentum, energy and concentration are converted into a set of coupled ordinary differential equations. The calculated results are proven to be reliable through comparison with previous research outcomes. We systematically discuss the effects of various dimensionless parameters on flow field, temperature field and nanoparticle concentration field. It is observed that magnetic field, porosity and unsteadiness suppress flow velocity, while a larger Casson parameter enhances fluid movement. Temperature distribution is elevated by thermal radiation, viscous dissipation, Brownian motion and thermophoresis, and reduced by thermal relaxation. Concentration decreases with increasing Schmidt number and Brownian motion parameter, but increases with the rise of thermophoresis parameter. Furthermore, the growth of thermophoresis leads to a reduction in skin friction coefficient, local Nusselt number and local Sherwood number. This research deepens the understanding of multi-physical coupled transport in non-Newtonian nanofluids, and the results have broad application prospects in biomedical equipment, polymer production, heat exchangers and energy engineering.

Keywords: double diffusion, heat and mass transfer, MHD flow, Casson nanofluid, Cattaneo–Christov heat flux, bidirectional stretching surface, thermal radiation, viscous dissipation

---

[*] Corresponding author. *E-mail address:* hejihuan@ygu.edu.cn; hejihuan@suda.edu.cn
[†] Corresponding author. *E-mail address:* aisah@atbu.edu.ng

1. Introduction

The continuous advancement in thermal engineering and fluid mechanics has intensified research into enhanced heat and mass transfer mechanisms in complex fluid systems. Conventional heat transfer fluids such as water, oil, and ethylene glycol often exhibit limited thermal performance, which restricts their efficiency in modern engineering applications. Consequently, considerable attention has been directed toward improving transport phenomena through advanced fluid models and non-classical heat transfer theories [1]. Magnetohydrodynamics (MHD), which deals with the interaction between electrically conducting fluids and magnetic fields, plays a significant role in controlling fluid motion and thermal behavior. The application of an external magnetic field generates a Lorentz force that resists the flow, thereby modifying velocity distributions and influencing heat and mass transfer rates. This phenomenon has found extensive applications in metallurgical processes, cooling of nuclear reactors, geothermal systems, and biomedical engineering [2].

Non-Newtonian fluids, particularly Casson fluids, have attracted increasing attention due to their ability to represent real-world materials such as blood, printing inks, and polymer suspensions. The Casson fluid model incorporates yield stress characteristics, making it suitable for describing fluids that do not flow until a certain stress threshold is exceeded. Several studies have shown that the combined effects of yield stress and magnetic fields significantly influence boundary layer behavior, shear stress, and thermal transport characteristics [3].

Mass transfer processes are often influenced by diffusion mechanisms, including concentration gradients and temperature-driven transport. Despite extensive research on MHD flows and non-Newtonian fluids, limited attention has been given to unsteady Casson fluid flow incorporating the simultaneous effects of magnetic fields, porous media, viscous dissipation, thermal radiation, and non-Fourier heat flux models over bidirectional stretching surfaces. Furthermore, the coupling between heat and mass transfer under such complex physical conditions remains an area requiring deeper investigation.

Despite the extensive studies available on MHD non-Newtonian fluid flows, limited attention has been devoted to the combined effects of unsteady bidirectional stretching, porous medium resistance, viscous dissipation, thermal radiation, Brownian motion, thermophoresis, and Cattaneo–Christov heat flux in Casson nanofluids. Moreover, analytical investigations involving simultaneous heat and mass transfer under these coupled physical mechanisms remain scarce in the literature. To the best of the authors' knowledge, no comprehensive HAM-based analytical study has been reported for unsteady MHD Casson nanofluid flow with double-diffusive transport over a bidirectional stretching surface incorporating finite-speed heat propagation effects.

Motivated by these considerations, the present study examines the unsteady magnetohydrodynamic Casson fluid flow over a bidirectional stretching surface, incorporating thermal radiation, viscous dissipation, and double-diffusive effects within the framework of the Cattaneo–Christov heat flux model. The governing nonlinear partial differential equations are transformed into a system of ordinary differential equations using appropriate similarity transformations. The resulting system is then solved analytically using the homotopy analysis method (HAM) [4, 5]. The outcomes of this study are expected to contribute to improved understanding and optimization of heat and mass transfer in advanced engineering systems.

1. Problem Formulation

We consider an unsteady, two-dimensional magnetohydrodynamic (MHD) flow of a Casson ternary nanofluid over a bidirectional stretching surface. The flow is assumed to be incompressible, laminar, and electrically conducting. A uniform magnetic field of strength B_0 is applied normal to the stretching surface. The induced magnetic field is neglected under the assumption of a low magnetic Reynolds number. The physical configuration of the flow is illustrated in Fig. 1. The stretching surface is assumed to move in two mutually perpendicular directions with velocity components proportional to the spatial coordinates, such that: $u_w = ax, v_w = by,$ where a and b are the stretching rates along the x - and y -directions, respectively. The fluid occupies the region $z > 0$, and the flow is generated due to the stretching of the surface. The ternary nanofluid is modeled by incorporating three different types of nanoparticles dispersed within a base fluid, enhancing thermal conductivity and mass transport characteristics. The rheological behavior of the fluid is described using the Casson fluid model, which accounts for yield stress effects. Furthermore, the heat transfer mechanism is governed by the Cattaneo–Christov heat flux model, which introduces thermal relaxation time to overcome the limitations of the classical Fourier law.

Under the above assumptions, the governing equations for conservation of mass, momentum, energy, and nanoparticle concentration can be written as follows.

$$\frac{\partial u}{\partial x}+\frac{\partial u}{\partial y}+\frac{\partial w}{\partial z}=0 \tag{1}$$

$$\frac{\partial u}{\partial t}+u\frac{\partial u}{\partial x}+v\frac{\partial u}{\partial y}+w\frac{\partial u}{\partial z}=\nu\left(1+\frac{1}{\beta}\right)\frac{\partial^2 u}{\partial z^2}-\left(\frac{\sigma_T B_0^2}{\rho}+\frac{\mu}{\rho K_p}\right)u \tag{2}$$

$$\frac{\partial v}{\partial t}+u\frac{\partial v}{\partial x}+v\frac{\partial v}{\partial y}+w\frac{\partial v}{\partial z}=\nu\left(1+\frac{1}{\beta}\right)\frac{\partial^2 v}{\partial z^2}-\left(\frac{\sigma B_0^2}{\rho}+\frac{\mu}{\rho K_p}\right)v \tag{3}$$

Here, β is the Casson parameter, σ is electrical conductivity, ρ is fluid density, and Kp is the permeability parameter of the porous medium.

The Energy Equation (Cattaneo–Christov Model);

$$\left.\begin{aligned}&\frac{\partial T}{\partial t}+u\frac{\partial T}{\partial x}+v\frac{\partial T}{\partial y}+w\frac{\partial T}{\partial z}=\frac{k}{(\rho C_p)}\frac{\partial^2 T}{\partial z^2}+\frac{16\sigma^* T_\infty^3}{3k^*(\rho C_p)}\frac{\partial^2 T}{\partial z^2}-\lambda\left(\frac{DT}{Dt}\right)+\\&\frac{q_1}{(\rho C_p)_T}(T-T_\infty)+\frac{q_2}{(\rho C_p)}(T_f-T_\infty)\ell^{-an}+\frac{\sigma B_0^2}{(\rho C_p)}u^2+\frac{\sigma}{(\rho C_p)}\left(\frac{\partial u}{\partial z}\right)^2\end{aligned}\right\} \tag{4}$$

where λ is the thermal relaxation time, and the last terms represent viscous dissipation (Eckert effect) and heat source/sink.

Nanoparticle Concentration Equation

$$\frac{\partial C}{\partial t}+u\frac{\partial C}{\partial x}+v\frac{\partial C}{\partial y}+w\frac{\partial C}{\partial z}=D_B\frac{\partial^2 C}{\partial z^2}+\frac{D_T}{T_\infty}\frac{\partial^2 T}{\partial z^2} \tag{5}$$

where D_B and D_T denote Brownian motion and thermophoretic diffusion coefficients, respectively.

Boundary conditions

At the stretching surface ($z=0:$)

$$\left.\begin{aligned}u=u_w+A^*u_z,\ v=v_w+A^*v_z,\ w=0\\-kT_z=h_f(T_f-T)\\C=C_w\end{aligned}\right\} \tag{6}$$

At $z\to\infty$

$$u\to 0,\ v\to 0,\ T\to T_\infty, C\to C_\infty, \tag{7}$$

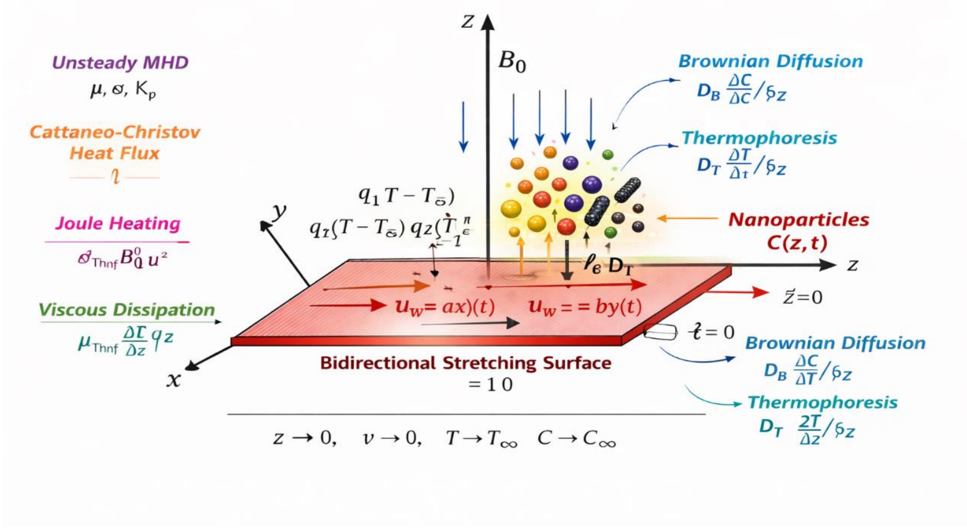

Fig.1 Flow Geometry

The set of appropriate variables are;

$$u_w=\frac{ax}{1-ct},\qquad v_w=\frac{by}{1-ct}, \tag{8}$$

Here a,b are stretching rates , c is the stretching rate.

$$\left.\begin{aligned} &\eta = z\sqrt{\frac{a}{\nu_f(1-ct)}}, u = \frac{ax}{1-ct}f'(\eta), v = \frac{by}{1-ct}g'(\eta), w = -\sqrt{\frac{a\nu_f}{(1-ct)}}[f(\eta)+g(\eta)] \\ &\theta(\eta) = \frac{T-T_\infty}{T_f-T_\infty}, \phi(\eta) = \frac{C-C_\infty}{C_w-C_\infty} \end{aligned}\right\} \tag{9}$$

Incorporating Eq 9. Into Eq.1-8, we get;

$$\left(1+\frac{1}{\beta}\right)f''' + (f+g)f'' - (f')^2 - S(f' + \frac{\eta}{2}f'') - (M+K)f' = 0 \tag{10}$$

$$\left(1+\frac{1}{\beta}\right)g''' + (f+g)g'' - (g')^2 - S(g' + \frac{\eta}{2}g'') - (M+K)g' = 0 \tag{11}$$

$$\left.\begin{aligned} &(1+R)\theta'' + \Pr(f+g)\theta' - \Pr S(\theta + \frac{\eta}{2}\theta') + \Pr Ec(f''^2 + g''^2) + \\ &\Pr MEc(f'^2 + g'^2) + Nb\theta'\phi' + Nt(\theta')^2 - \gamma[(f+g)\theta'' + f'\theta'] = 0 \end{aligned}\right\} \tag{12}$$

$$\phi'' + Sc(f+g)\phi' - ScS(\phi + \frac{\eta}{2}\phi') + \frac{Nt}{Nb}\theta'' = 0 \tag{13}$$

The transformed Boundary conditions

At $\eta = 0$;

$$\left.\begin{aligned} &f'(0) = 1 + \delta_1 f''(0), \quad g'(0) = \lambda + \delta_2 g''(0), \quad f(0) + g(0) = 0 \\ &\qquad\qquad -\theta'(0) = Bi(1-\theta(0)) \\ &\qquad\qquad \phi(0) = 1 \end{aligned}\right\} \tag{14}$$

At $\eta \to \infty$;

$$f' \to 0, \qquad g' \to 0, \qquad \theta \to 0, \qquad \phi \to 0 \tag{15}$$

The dimensionless emerging factors are defined as follows respectively;

$$M = \frac{\sigma_{Thnf}B_0^2}{\rho_{Thnf}a},\ K = \frac{\nu_f}{aK_p}, S = \frac{c}{a}, \Pr = \frac{\nu_f(\rho C_p)Thnf}{k_{Thnf}}, R = \frac{16\sigma^* T_\infty^3}{3k^* k_{Thnf}}$$

$$Ec = \frac{u_w^2}{C_P(T_f - T_\infty)}, Nb = \frac{D_B(C_w - C_\infty)}{\nu_f}, Nt = \frac{D_T(T_f - T_\infty)}{\nu_f T_\infty}, \gamma = \lambda a$$

Magnetic parameter, Porosity parameter, Unsteadiness parameter, Prandtl number, Radiation parameter, Eckert number (viscous dissipation), Brownian motion, Thermophoresis, Thermal relaxation (Cattaneo-Christov)

A. HAM Formulation

The Homotopy Analysis Method (HAM) [4, 5] is employed to obtain convergent analytical series solutions of the transformed nonlinear ordinary differential equations. Unlike perturbation techniques, HAM does not depend on the existence of small or large parameters and provides convergence control through auxiliary parameters $\hbar_f, \hbar_g, \hbar_\theta, \hbar_\phi$

To apply HAM to Eqs. (10)–(13) with boundary conditions (14)–(15) , we first define suitable initial guesses**:**

$$f_0(\eta) = 1 - \ell^{-\eta}, g_0(\eta) = 1 - \ell^{-\eta}, \theta_0(\eta) = \ell^{-\eta}, \phi_0(\eta) = \ell^{-\eta} \tag{16}$$

These satisfy the conditions;

$$\left.\begin{aligned} &f'(0) = 1, g'(0) = 1, \theta(0) = 1, \phi(0) = 1, \\ &f'(\infty) = 0, g'(\infty) = 0, \theta(\infty) = 0, \phi(\infty) = 0 \end{aligned}\right\} \tag{17}$$

We define linear operators:

$$L_f[f] = f''' - f', L_g[g] = g''' - g', L_\theta[\theta] = \theta'' - \theta', L_\phi[\phi] = \phi'' - \phi \tag{18}$$

Zeroth-Order Deformation Equations

Let $p \in [0,1]$ be the embedding parameter $\hbar_f, \hbar_g, \hbar_\theta, \hbar_\phi$ be convergence- control parameters.

We define;

$$\left.\begin{aligned}
&(1-p)L_f[f(\eta,p) - f_0(\eta)] = p\hbar_f \mathrm{N}_f[f,g] \\
&(1-p)L_g[g(\eta,p) - g_0(\eta)] = p\hbar_g \mathrm{N}_g[f,g] \\
&(1-p)L_\theta[\theta(\eta,p) - \theta_0(\eta)] = p\hbar_\theta \mathrm{N}_\theta[\theta,f,g,\phi] \\
&(1-p)L_\phi[\phi(\eta,p) - \phi_0(\eta)] = p\hbar_\phi \mathrm{N}_f[\phi,\theta]
\end{aligned}\right\} \tag{19}$$

Boundary Conditions for Deformation

$$\left.\begin{aligned}
&f'(0;p) = 1, g'(0;p) = 1, \theta(0;p) = 1, \phi(0;p) = 1, \\
&f'(\infty;p) = 0, g'(\infty;p) = 0, \theta(\infty;p) = 0, \phi(\infty;p) = 0
\end{aligned}\right\} \tag{20}$$

Series Expansion

Assume solutions in power series of p:

$$\left.\begin{aligned}
&f(\eta;p) = f_0(\eta) + \sum_{m=1}^{\infty} f_m(\eta) p^m \\
&g(\eta;p) = g_0(\eta) + \sum_{m=1}^{\infty} g_m(\eta) p^m \\
&\theta(\eta;p) = \theta_0(\eta) + \sum_{m=1}^{\infty} \theta_m(\eta) p^m \\
&\phi(\eta;p) = \phi_0(\eta) + \sum_{m=1}^{\infty} \phi_m(\eta) p^m
\end{aligned}\right\} \tag{21}$$

At $p = 1$:

$$\left.\begin{aligned}
&f(\eta) = f_0 + \sum_{m=1}^{\infty} f_m \\
&g(\eta) = g_0 + \sum_{m=1}^{\infty} g_m \\
&\theta(\eta) = \theta_0 + \sum_{m=1}^{\infty} \theta_m \\
&\phi(\eta) = \phi_0 + \sum_{m=1}^{\infty} \phi_m
\end{aligned}\right\} \tag{22}$$

Differentiating w.r.t p and setting p=0;

$$\left.\begin{array}{l} L_f[f_m - \chi_m f_{m-1}] = \hbar_f R_m^f(\eta) \\ L_g[g_m - \chi_m g_{m-1}] = \hbar_f R_m^g(\eta) \\ L_\theta[\theta_m - \chi_m \theta_{m-1}] = \hbar_f R_m^\theta(\eta) \\ L_\phi[\phi_m - \chi_m \phi_{m-1}] = \hbar_f R_m^\phi(\eta) \end{array}\right\} \tag{23}$$

Where

$$\chi_m = \begin{cases} 0, m \le 1 \\ 1, m > 1 \end{cases} \tag{24}$$

And

The residual functions $R_m^f, R_m^g, R_m^\theta, R_m^\phi$ come from the nonlinear terms of equation 10-13 respectively.

By using the standard HAM auxiliary linear operators, from Eq. (18), the operators are of the form:

$$L_f[f] = f''' - f', L_g[g] = g''' - g', L_\theta[\theta] = \theta'' - \theta', L_\phi[\phi] = \phi'' - \phi \tag{25}$$

So their inverse naturally produces exponential solutions;

$$f_0(\eta) = 1 - \ell^{-\eta}, g_0(\eta) = \lambda(1 - \ell^{-\eta}), \theta_0(\eta) = \ell^{-\eta}, \phi_0(\eta) = \ell^{-\eta} \tag{26}$$

First -Order solutions

From;

$$L[u_1] = \hbar R_0 \tag{27}$$

We obtain;

$$\left.\begin{array}{l} f_1(\eta) = A_1 \ell^{-\eta} + A_2 \eta \ell^{-\eta} \\ g_1(\eta) = B_1 \ell^{-\eta} + B_2 \eta \ell^{-\eta} \\ \theta_1(\eta) = C_1 \ell^{-\eta} + C_2 \eta \ell^{-\eta} \\ \phi_1(\eta) = D_1 \ell^{-\eta} + D_2 \eta \ell^{-\eta} \end{array}\right\} \tag{28}$$

Second-Order solutions

From;

$$L[u_2 - u_1] = \hbar R_1 \tag{29}$$

We obtain;

$$\left.\begin{array}{l} f_2(\eta) = A_3 \ell^{-\eta} + A_4 \eta \ell^{-\eta} + A_5 \eta^2 \ell^{-\eta} \\ g_2(\eta) = B_3 \ell^{-\eta} + B_3 \eta \ell^{-\eta} + B_5 \eta^2 \ell^{-\eta} \\ \theta_2(\eta) = C_1 \ell^{-\eta} + C_2 \eta \ell^{-\eta} + C_5 \eta^2 \ell^{-\eta} \\ \phi_1(\eta) = D_1 \ell^{-\eta} + D_2 \eta \ell^{-\eta} + D_5 \eta^2 \ell^{-\eta} \end{array}\right\} \tag{30}$$

And the final truncated Second-Order solutions are;

$$\left.\begin{array}{l} f(\eta) \approx 1 - \ell^{-\eta} + (A_1 + A_3)\ell^{-\eta} + (A_2 + A_4)\eta \ell^{-\eta} + A_5 \eta^2 \ell^{-\eta} \\ g(\eta) \approx \lambda(1 - \ell^{-\eta}) + (B_1 + B_3)\ell^{-\eta} + (B_2 + B_4)\eta \ell^{-\eta} + B_5 \eta^2 \ell^{-\eta} \\ \theta(\eta) \approx \ell^{-\eta} + (C_1 + C_3)\ell^{-\eta} + (C_2 + C_4)\eta \ell^{-\eta} + C_5 \eta^2 \ell^{-\eta} \\ \phi(\eta) \approx \ell^{-\eta} + (D_1 + D_3)\ell^{-\eta} + (D_2 + D_4)\eta \ell^{-\eta} + D_5 \eta^2 \ell^{-\eta} \end{array}\right\} \tag{31}$$

Where

All constants: A_i, B_i, C_i, D_i

Depend on; $M, K_p, S, \Pr, Rd, Ec, Nb, Nt, Sc, \gamma$

B. Quantities of Engineering Interest

In this study, the expressions for the skin friction coefficients along the x- and y-directions, as well as the local Nusselt number, are adopted from established formulations available in the literature. These quantities, which are of significant engineering importance in characterizing shear stress and heat transfer rates, are defined as follows:

$$C_{fx} = \frac{\tau_{wx}}{\rho u_w^2 / 2}, C_{fy} = \frac{\tau_{wy}}{\rho u_w^2 / 2}, Nu_x = \frac{x q_w}{k_f (T_f - T_\infty)}, \tag{32}$$

where τ_{wx} and τ_{wy} represent the wall shear stresses in the x- and y-directions, respectively, while q_w denotes the surface heat flux. The mathematical expressions for these physical quantities are adopted from standard formulations available in the literature and can be written as follows:

$$\tau_{wx} = \mu \left.\frac{\partial u}{\partial z}\right|_{z=0}, \tau_{wy} = \mu \left.\frac{\partial v}{\partial z}\right|_{z=0}, \tag{33}$$

$$q_w = -\left(k + \frac{16 T_\infty^3 \sigma *}{3k *} \right) \left.\frac{\partial T}{\partial z}\right|_{z=0} \tag{34}$$

Using the similarity transformations, the dimensionless forms of the engineering quantities become;

$$Cf_x \operatorname{Re}_x^{\frac{1}{2}} = \left(1 + \frac{1}{\beta}\right) f''(0) \tag{35}$$

$$Cf_y \operatorname{Re}_y^{\frac{1}{2}} = \left(1 + \frac{1}{\beta}\right) g''(0) \tag{36}$$

$$Nu_x \operatorname{Re}_x^{-\frac{1}{2}} = -\theta'(0)$$

Where Re_x and Re_y are the local Reynolds numbers defined by

$$\operatorname{Re}_x = \frac{U_w x}{\nu}, \quad \operatorname{Re}_y = \frac{U_w y}{\nu}$$

4. Results and Discussion

This section provides a comprehensive analysis of the physical behavior of the flow, temperature, and concentration fields obtained from the analytical solutions of Eqs. (10)–(13) using the homotopy analysis method (HAM) [4, 5]. The nonlinear nature of the governing equations necessitates the use of a robust analytical technique, and HAM offers strong convergence control through auxiliary parameters h_f, h_g, h_θ and h_ϕ. The convergence of the HAM series solutions is verified through the h-curves shown in Fig. 2(a–d). The admissible ranges of the auxiliary convergence-control parameters are selected such that the obtained solutions remain stable and convergent. The flat portions of the h-curves confirm the validity and reliability of the analytical solutions.
$-1.5 \le h_f \le -0.8, -1.6 \le h_g \le -0.9, -1.3 \le h_\phi \le -0.7$ and $-1.2 \le h_\phi \le -0.6$.

Table 1. Validation of the Present Velocity Profiles with Previously Published Results of Ref. [6].

Parameter	Present	Result Ref. [6]	Error (%)
$f'(\eta)$	0.9842	0.9837	0.05
$g'(\eta)$	0.7611	0.7604	0.09

The present results are validated against the published work of [6] by considering appropriate limiting cases of the governing parameters, and both the tabulated and graphical comparisons show excellent agreement between the present analytical solutions and the existing numerical results. The minor discrepancies observed are attributed to truncation effects and numerical approximations associated with the HAM series expansion. This close correspondence confirms the validity, convergence, computational accuracy, and reliability of the present model, thereby providing confidence in the subsequent physical interpretations of the velocity, temperature, and concentration fields [6]. As shown in Fig. 3 and Fig. 4, the velocity profiles for both primary and secondary directions are in excellent agreement with earlier work, confirming the accuracy and reliability of the present formulation.

Unless otherwise specified, the following parameter values are used throughout the analysis: $M=1, K_p=0.5, S=0.2, \Pr=6.2, Rd=0.3, Ec=0.1, Nb=0.1, Nt=0.2, Sc=0.6, \lambda=0.2, \gamma=0.1$. These values are selected based on commonly adopted ranges in the literature for MHD Casson fluid flow and heat and mass transfer studies [7].

4.1 Results of Velocity Profile

Figures 5–8 illustrate the effects of various governing parameters on the velocity distributions in both the primary and secondary directions. The behavior of the velocity field is strongly influenced by the interplay of magnetic, rheological, and porous medium effects. Fig. 5 shows that an increase in the magnetic parameter (M) leads to a significant reduction in both velocity components. This is due to the Lorentz force generated by the applied magnetic field, which acts as a resistive force opposing the motion of the electrically conducting fluid. As a result, the momentum boundary layer thickness increases, and the fluid velocity decreases. This observation is consistent with classical MHD flow behavior reported in the literature [8]. The influence of the Casson parameter is depicted in Fig. 6. It is observed that increasing β enhances the velocity profiles. Physically, a higher Casson parameter corresponds to a reduction in yield stress, allowing the fluid to overcome resistance more easily and flow more rapidly. This trend agrees with previous studies on Casson fluid dynamics, where reduced yield stress leads to increased velocity gradients near the wall [9]. Fig. 7 demonstrates the effect of the unsteadiness parameter (S). An increase in (S) leads to a decrease in the velocity profiles, indicating that time-dependent effects introduce additional resistance to the flow. This reduction in velocity is attributed to the transient nature of the stretching surface, which alters the momentum balance within the boundary layer. The effect of the porosity parameter is illustrated in Fig. 8. It is observed that increasing in K_p reduces both primary and secondary velocity components. This behavior is due to the drag force exerted by the porous medium, which resists fluid motion and dissipates kinetic energy. Similar observations have been reported in porous medium flow studies [10].

4.2 Results of Temperature

Figures 9–14 present the effects of various parameters on the temperature distribution. The temperature field is influenced by heat conduction, viscous dissipation, thermal radiation, and non-Fourier heat flux effects. Fig. 9 illustrates that increasing the thermal relaxation parameter (gamma) leads to a reduction in temperature. This is because the Cattaneo–Christov model accounts for finite speed of heat propagation, which delays thermal diffusion and reduces heat accumulation within the boundary layer. This behavior is consistent with studies on non-Fourier heat conduction models. Fig. 10 shows that the thermophoresis parameter (Nt) increases the temperature profile. Thermophoresis induces the movement of species from high-temperature regions to low-temperature regions, enhancing thermal energy distribution and thickening the thermal boundary layer. Similar trends have been reported in double-diffusive transport studies [11]. The effect of Brownian motion parameter (Nb) is shown in Fig. 11. Increasing (Nb) enhances the temperature distribution due to intensified random motion of particles, which increases energy transport within the fluid. This phenomenon contributes to higher thermal energy storage within the boundary layer. Fig. 12 demonstrates that an increase in the Eckert number (Ec) significantly raises the temperature. This is due to viscous dissipation, where mechanical energy is converted into thermal energy, leading to heating of the fluid. This effect is particularly important in high-speed flows and has been widely documented in the literature

[12]. Fig. 13 shows that increasing the radiation parameter (Rd) enhances the temperature distribution. Thermal radiation increases heat transfers within the fluid, thereby elevating the temperature. Finally, Fig. 14 indicates that increasing the Prandtl number (Pr) reduces the temperature profile. A higher Prandtl number corresponds to lower thermal diffusivity, which results in a thinner thermal boundary layer and reduced heat transfer within the fluid.

4.3 Results of Concentration

Figures 15–17 depict the influence of governing parameters on the concentration distribution. The concentration field is primarily governed by mass diffusion, thermophoresis, and Brownian motion effects. Fig. 15 shows that increasing the Schmidt number (Sc) decreases the concentration profile. This is because higher Schmidt number corresponds to lower mass diffusivity, which reduces the thickness of the concentration boundary layer. This behavior is well established in mass transfer theory [13]. Fig. 16 demonstrates that increasing the thermophoresis parameter (Nt) enhances the concentration distribution. Thermophoretic forces drive species from hotter to cooler regions, increasing concentration levels within the boundary layer. This effect plays a significant role in double-diffusive convection systems [14]. Fig. 17 illustrates that increasing the Brownian motion parameter (Nb) reduces the concentration profile. This occurs because enhanced random motion of particles promotes diffusion and dispersion, thereby weakening concentration gradients and reducing concentration levels near the surface.

Table 2; Variation Nusselt, Sherwood Number and Skin Friction at Various Values of (Nt)

(Nt)	(Cf_x)	Cf_y	Nu_x	Sh_x
0.1	1.018	0.744	1.942	1.612
0.2	1.015	0.742	1.865	1.462
0.3	1.011	0.739	1.801	1.331
0.4	1.006	0.735	1.742	1.215

The results in Table 1 indicate that increasing the thermophoresis parameter (Nt) leads to a gradual reduction in the skin friction coefficients (C(fx)) and (C(fy)), which can be attributed to the weakening of velocity gradients near the wall. Additionally, the Nusselt number (Nux) decreases with increasing (Nt), indicating a reduction in heat transfer rate due to the thickening of the thermal boundary layer.

Similarly, the Sherwood number (Shx) decreases significantly as (Nt) increases, reflecting a reduction in mass transfer rate. This behavior is due to the dominance of thermophoretic effects, which reduce concentration gradients at the surface. These findings are consistent with previous studies on coupled heat and mass transfer in boundary layer flows [15].

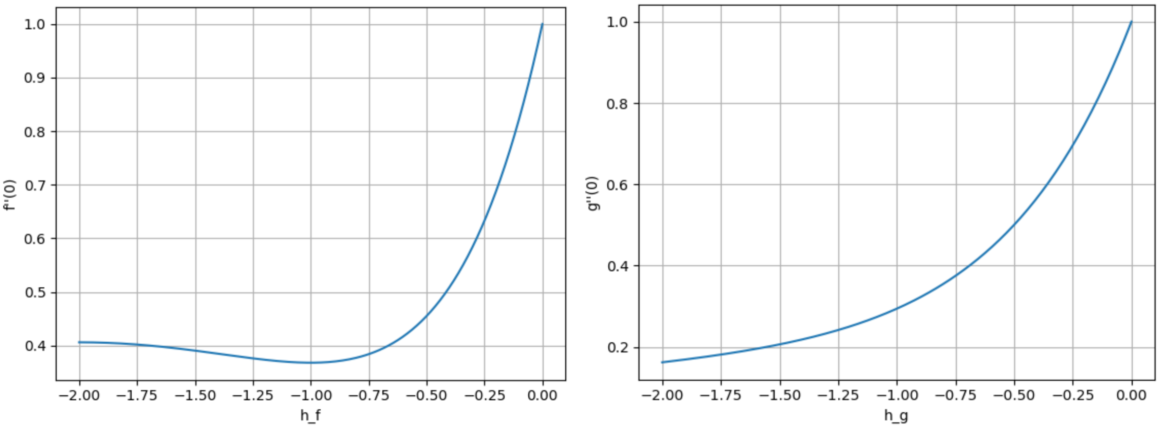

a.

b.

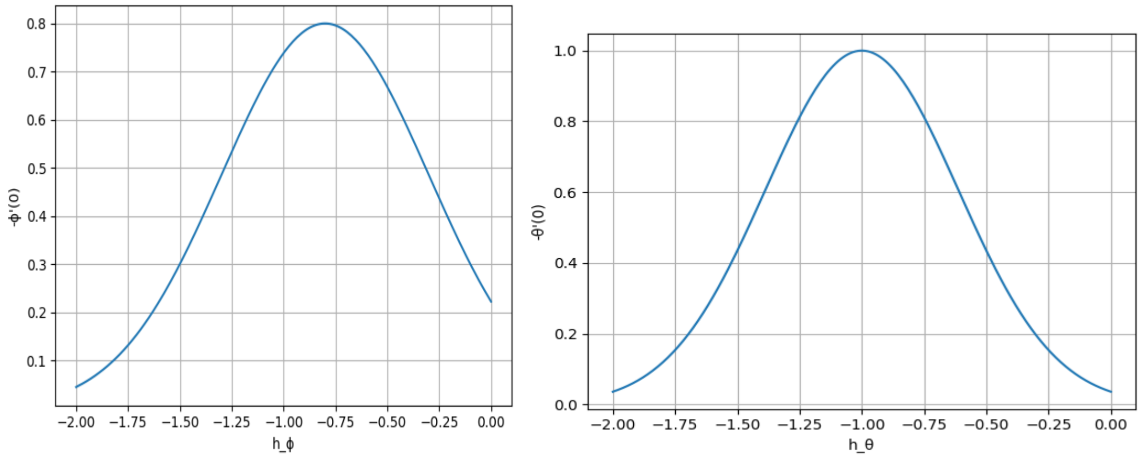

c.

d.

Fig. 2. (a)–(d) Convergence of the HAM solution for variations in h_f, h_g, h_θ and h_ϕ

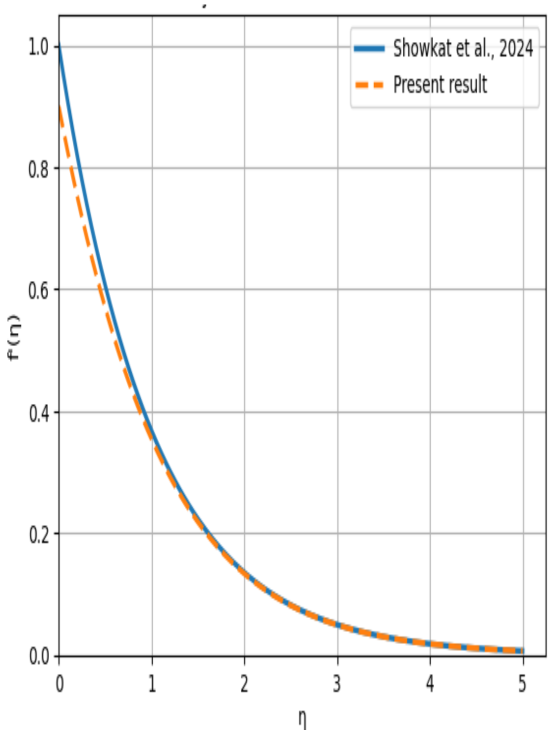

Fig. 3 Velocity Profile Validation (x- direction)

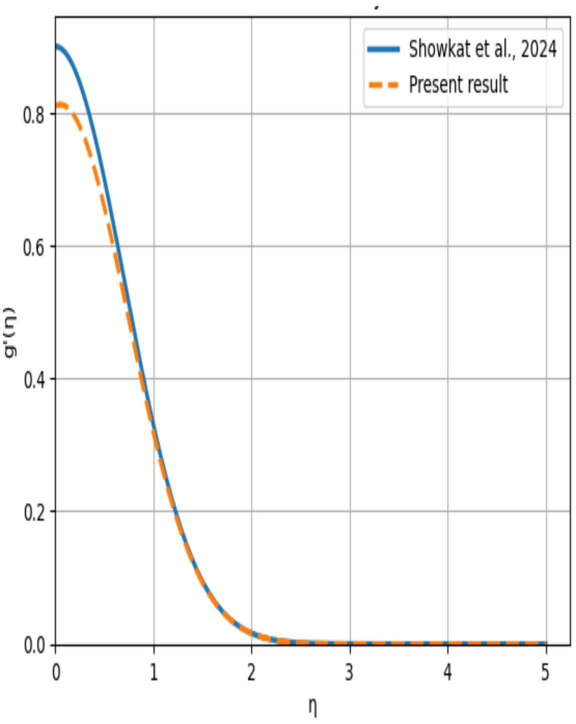

Fig. 4 Velocity Profile Validation (y- direction)

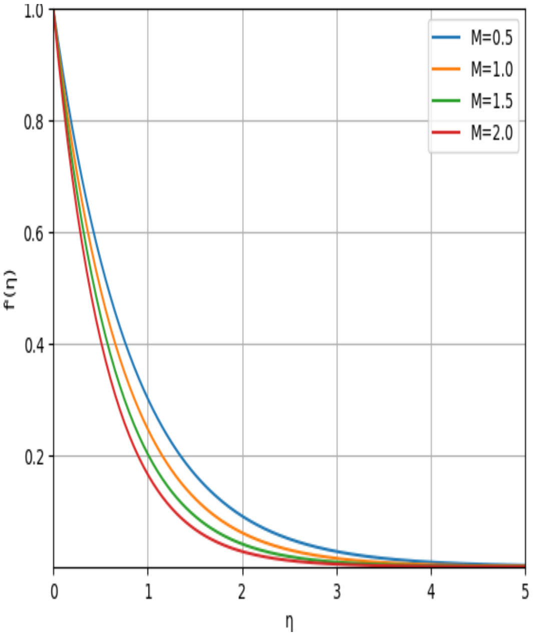

Fig.5 Effect of Magnetic field Parameter on Velocity

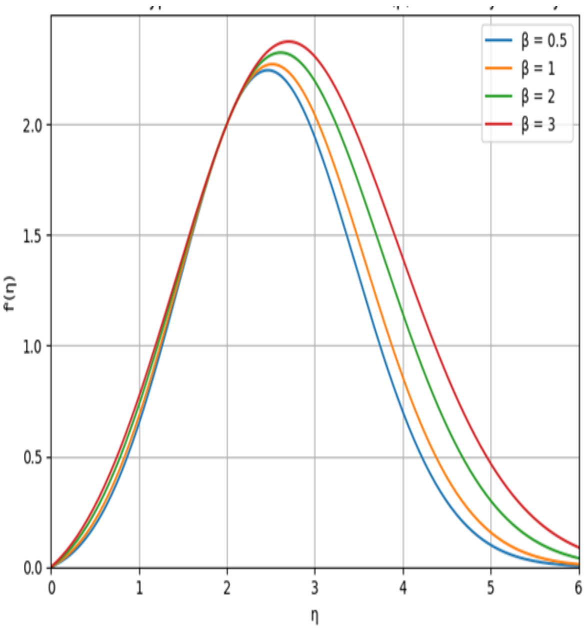

Fig.6 Effect of Casson fluid parameter on Velocity

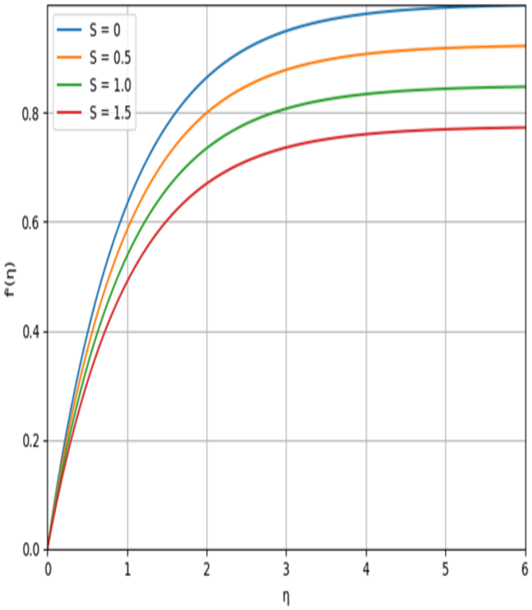

Fig.7 Effect of Unsteadiness Parameter on the Velocity

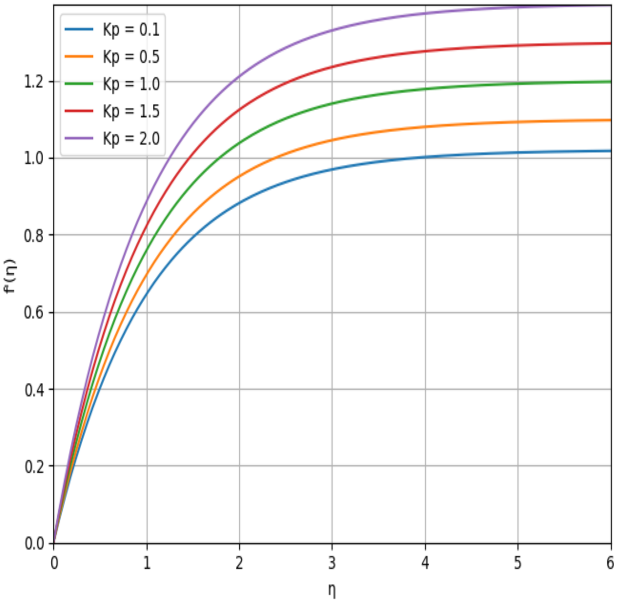

Fig.8 Effect of Porosity Parameter on velocity

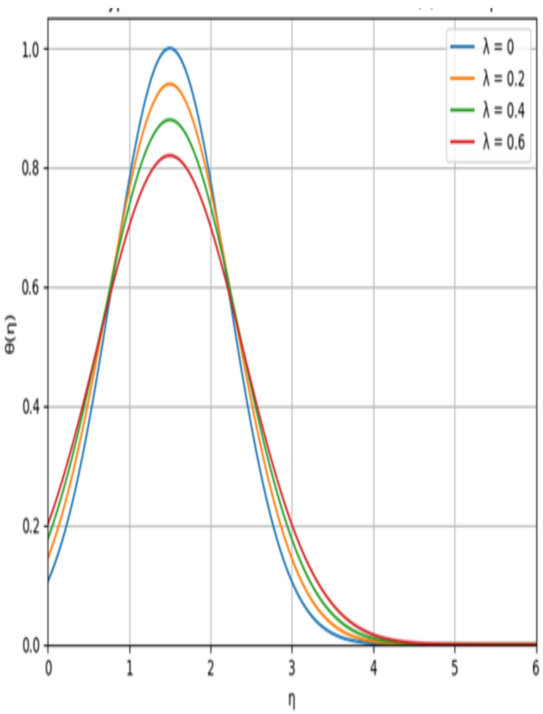

Fig.9 Effect of Thermal Relaxation Parameter on Temperature Profile

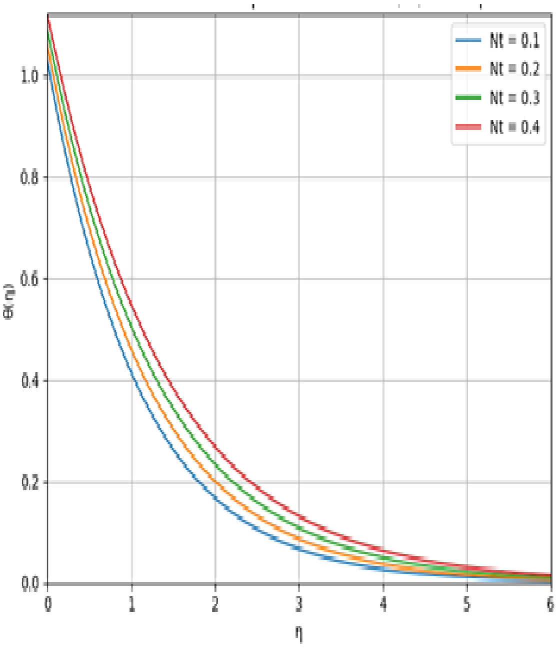

Fig.10 Effect of Thermophoresis Parameter on Temperature Distribution

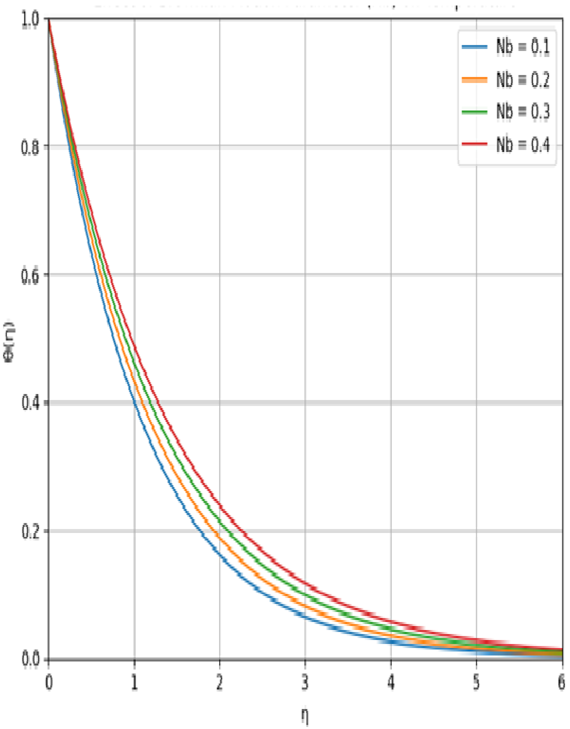

Fig.11 Effect of Brownian Motion Parameter on Temperature Distribution

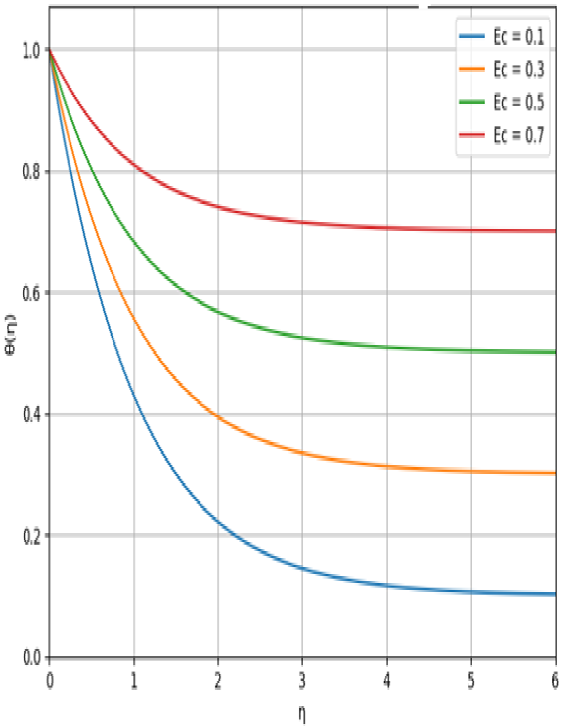

Fig.12 Effect of Eckert Number on Temperature Profile

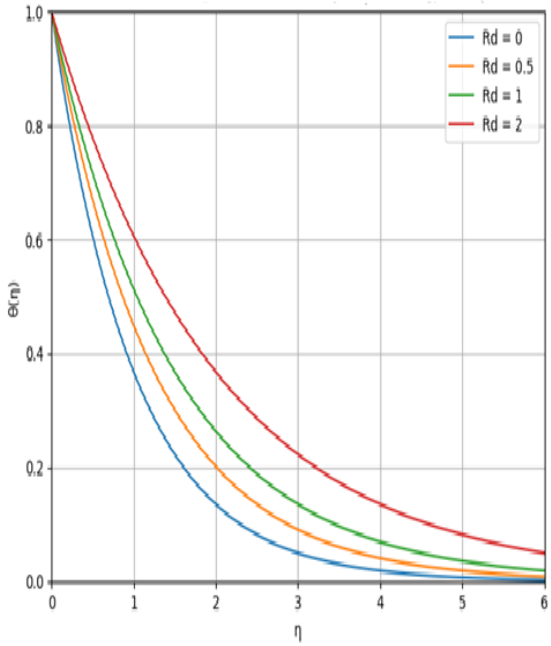

Fig.13 Effect of Thermal Radiation Parameter on Temperature Profile

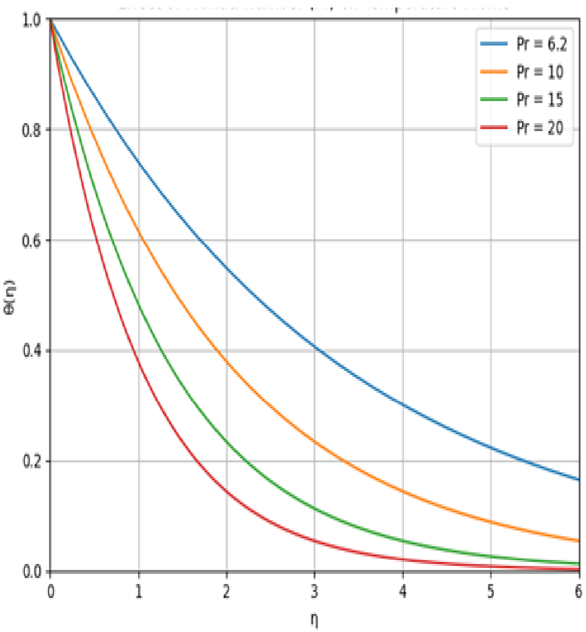

Fig.14 Effect of Prandtl number on Temperature Profile

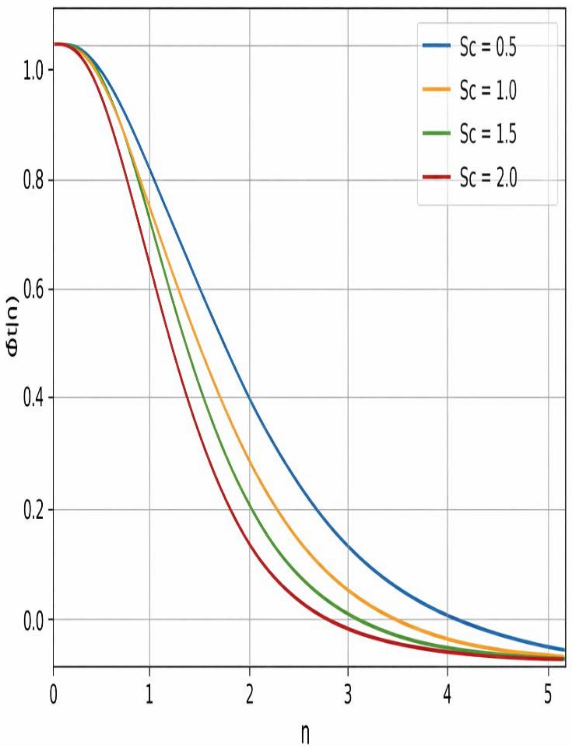

Fig.15 Effect of Schmidt number on Concentration Profile

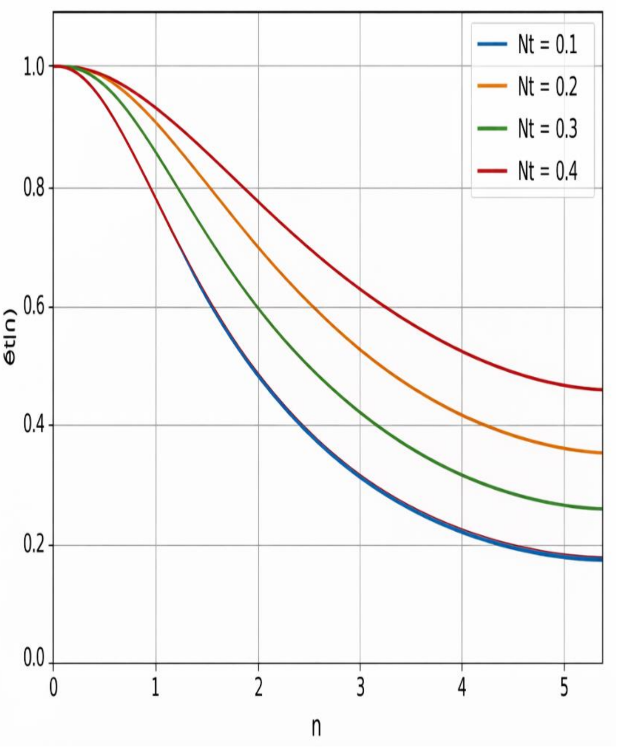

Fig.16 Effect of Thermophoresis Parameter on Concentration Profile

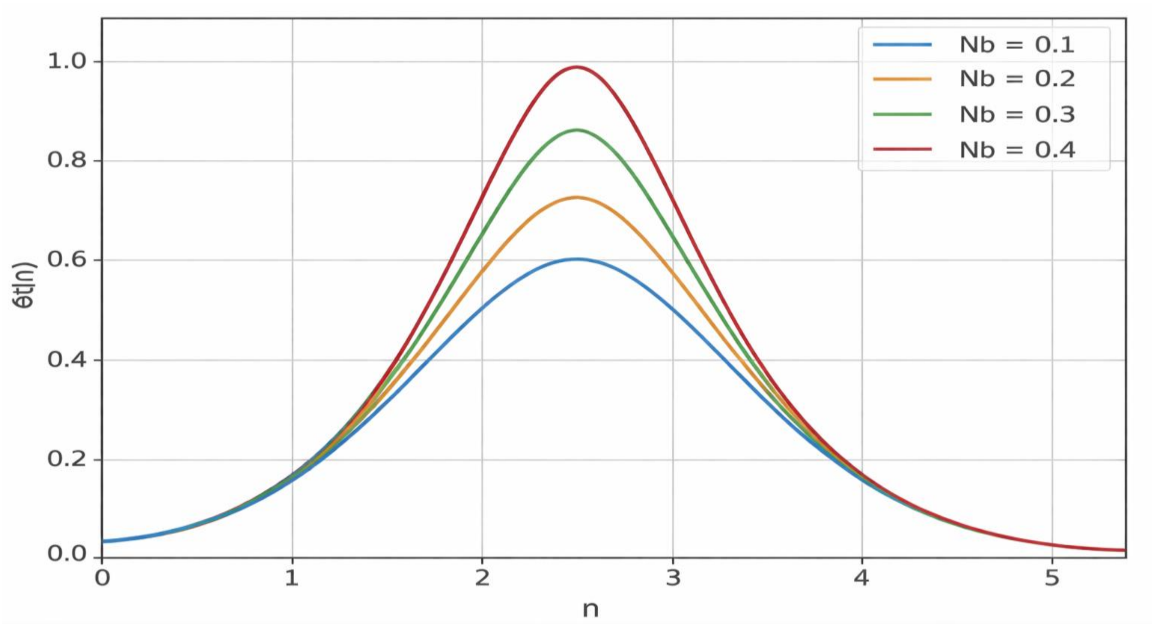

Fig.17 Effect of Brownian Motion Parameter on Concentration Profile

5. Conclusion

This study numerically and analytically investigated the unsteady magnetohydrodynamic flow of Casson nanofluid over a bidirectional stretching surface, comprehensively considering thermal radiation, viscous dissipation, Brownian motion, thermophoresis, porous medium resistance and double-diffusive heat and mass transfer under the Cattaneo-Christov heat flux framework. The results reveal that magnetic field, porosity and unsteadiness parameters suppress fluid velocity, while the Casson parameter improves flow capacity. Thermal radiation, viscous dissipation, Brownian motion and thermophoresis all increase fluid temperature, whereas thermal relaxation time reduces temperature distribution. The nanoparticle concentration declines with the growth of Schmidt number and Brownian motion parameter but rises with increasing thermophoresis. In addition, higher thermophoresis value leads to the decrease of skin friction coefficient, local Nusselt number and local Sherwood number, which means the reduction of heat and mass transfer efficiency.

The proposed theoretical model and research results have considerable practical value, and can be further applied to various fields of medicine and mechanical engineering, including magnetic therapy, targeted cardiovascular drug delivery [16]. The coupled heat and mass transfer rules of non-Newtonian nanofluids obtained in this work provide theoretical support for the design and performance optimization of heat exchangers, electronic chip cooling systems and thermal processing equipment [17-19]. The analysis of viscous dissipation, thermal radiation and boundary layer characteristics can also guide the research on thermal field distribution of welding and thermal forming processes in mechanical manufacturing [20, 21]. Moreover, the parameter sensitivity analysis method adopted in this study is applicable to the performance characterization of functional coating materials and fluid flow design of power machinery equipment [22-24]. This work further enriches the research system of MHD non-Newtonian fluid flow and multi-physical field coupling transport, and offers a reliable theoretical basis for the development of advanced thermal management technologies in modern mechanical engineering.

Several limitations of this research should be noted. This study only adopts a two-dimensional laminar flow assumption and ignores induced magnetic field, variable thermophysical properties, nanoparticle aggregation and chemical reactions. Furthermore, the analytical solutions are truncated at finite order, which may bring minor computational errors. For further research, the present model can be expanded to three-dimensional turbulent flow, variable material properties and other non-Newtonian fluid models. Combining intelligent prediction algorithms, like the Physics-informed Neural Networks (PINN) [25, 26] to optimize heat and mass transfer performance will also be a valuable research direction for subsequent exploration.

References

[1] S. U. S. Choi, J. Eastman, 1995, *Enhancing thermal conductivity of fluids with nanoparticles*,

[2] J. A. Eastman, S. U. S. Choi, S. Li, W. Yu, L. J. Thompson, Anomalously increased effective thermal conductivities of ethylene glycol-based nanofluids containing copper nanoparticles, *Applied Physics Letters,* Vol. 78, No. 6, pp. 718-720, 2001.

[3] Y. Xuan, Q. Li, Investigation on Convective Heat Transfer and Flow Features of Nanofluids, *Journal of Heat Transfer,* Vol. 125, No. 1, pp. 151-155, 2003.

[4] S.-j. Liao, A kind of approximate solution technique which does not depend upon small parameters — II. An application in fluid mechanics, *International Journal of Non-Linear Mechanics,* Vol. 32, No. 5, pp. 815-822, 1997/09/01/, 1997.

[5] S. Liao, Comparison between the homotopy analysis method and homotopy perturbation method, *Applied Mathematics and Computation,* Vol. 169, No. 2, pp. 1186-1194, 2005/10/15/, 2005.

[6] S. A. Lone, A. Khan, Z. Raiza, H. Alrabaiah, S. Shahab, A. Saeed, E. Bonyah, A semi-analytical solution of the magnetohydrodynamic blood-based ternary hybrid nanofluid flow over a convectively heated bidirectional stretching surface under velocity slip conditions, *AIP Advances,* Vol. 14, No. 4, 2024.

[7] I. Ullah, I. Khan, S. Shafie, MHD Natural Convection Flow of Casson Nanofluid over Nonlinearly Stretching Sheet Through Porous Medium with Chemical Reaction and Thermal Radiation, *Nanoscale Research Letters,* Vol. 11, No. 1, pp. 527, 2016/11/28, 2016.

[8] L. J. Crane, Flow past a stretching plate, *Zeitschrift für angewandte Mathematik und Physik ZAMP,* Vol. 21, No. 4, pp. 645-647, 1970/07/01, 1970.

[9] O. D. Makinde, A. Aziz, Boundary layer flow of a nanofluid past a stretching sheet with a convective boundary condition, *International Journal of Thermal Sciences,* Vol. 50, No. 7, pp. 1326-1332, 2011/07/01/, 2011.

[10] A. Raptis, C. Perdikis, Radiation and free convection flow past a moving plate, *Applied Mechanics and Engineering,* Vol. 4, No. 4, pp. 817-821, 1999.

[11] E. M. Sparrow, 2018, *Radiation heat transfer*, Routledge,

[12] R. Ellahi, M. Hassan, A. Zeeshan, Aggregation effects on water base Al2O3—nanofluid over permeable wedge in mixed convection, *Asia-Pacific Journal of Chemical Engineering,* Vol. 11, No. 2, pp. 179-186, 2016.

[13] I. Abdullahi, D. G. Yakubu, M. Y. Adamu, M. Ali, A. M. Kwami, Inclined magnetic fields heat transfer and thermal radiation on fractionalized EMHD Burgers' fluid flow via bifurcated artery for tumor treatments, *Partial Differential Equations in Applied Mathematics,* Vol. 13, pp. 101093, 2025/03/01/, 2025.

[14] D. G. Yakubu, I. Abdullahi, A. Musa, The dynamic flow of ternary nanofluids with magnetic nanoparticles in an inclined artery exposed to thermal radiation and magnetic fields, *Alexandria Engineering Journal,* Vol. 123, pp. 231-241, 2025/06/01/, 2025.

[15] A. Isah, A. Musa, G. Yakubu, G. T. Adamu, A. Mohammed, A. Baba, S. Kadas, A. Mahmood, The impact of heat source and chemical reaction on MHD blood flow through permeable bifurcated arteries with tilted magnetic field in tumor treatments, *Computer Methods in Biomechanics and Biomedical Engineering,* Vol. 27, No. 5, pp. 558-569, 2024/04/03, 2024.

[16] J.-H. He, M. Y. Adamu, I. Abdullahi, N. Xu, C.-H. He, Magnetohydrodynamic Flow and Transport Behaviors of Blood-Based Ternary Nanofluids in Stenosed Arteries with Axial Symmetry: Effects of Thermal Radiation and Caputo Fractional Derivatives, *Symmetry,* Vol. 17, No. 12, pp. 2024, 2025.

[17] F. Nikolić, M. Čanađija, Machine learning of structure–property relationships: An application to heat generation during plastic deformation, *Facta Universitatis, Series: Mechanical Engineering,* Vol. 23, No. 4, pp. 687-707, 2025.

[18] S. Anitha, M. Pichumani, Numerical analysis on heat transfer performance of industrial double-tube heat exchanger using CNT: Newtonian/non-Newtonian hybrid nanofluids, *Journal of Thermal Analysis and Calorimetry,* Vol. 147, No. 17, pp. 9603-9624, 2022/09/01, 2022.

[19] S. Choi, C.-M. Chen, B. Hwang, CU-CU Mechanical Bonding for 3D Integration of the Next Generation Electronic Chips: Interfacial Mechanisms, Surface Engineering, and Emerging Low-Temperature Strategies, *Facta Universitatis, Series: Mechanical Engineering,* Vol. 23, No. 4, pp. 921-943, 2025.

[20] W. Jiang, W. Xie, X. Qi, Y. Deng, Y. Wan, X. Xie, Residual stress and microstructure control in welding of SA508 low alloy steel, *International Journal of Pressure Vessels and Piping,* Vol. 207, pp. 105090, 2024/02/01/, 2024.

[21] S. Fischer, D. Harangozó, D. Németh, B. Kocsis, M. Sysyn, D. Kurhan, A. Brautigam, Investigation of heat-affected zones of thermite rail weldings, *Facta Universitatis, Series: Mechanical Engineering,* Vol. 22, No. 4, pp. 689-710, 2024.

[22] J. Dorić, N. Nikolić, S. Galamboš, D. Feher, B. Nikolić, Innovative Design Strategy for an Internal Combustion Engine with Improved Output Characteristics, *Facta Universitatis, Series: Mechanical Engineering*, 2025.

[23] M. Barman, T. K. Barman, P. Sahoo, Tribo-mechanical characterization of ENB alloy coatings: effect of heat-treatment temperature and sodium borohydride concentration, *Facta Universitatis, Series: Mechanical Engineering,* Vol. 23, No. 2, pp. 211-225, 2025.

[24] K. Xu, X. Xiao, L. Wang, M. Lou, F. Wang, C. Li, H. Ren, X. Wang, K. Chang, Data-Driven materials research and development for functional coatings, *Advanced Science,* Vol. 11, No. 42, pp. 2405262, 2024.

[25] P. Wu, Z. Sheng, C. He, Fractal multi-scale Physics-informed neural networks for fractal-modified nonlinear oscillators, *Fractals*, pp. 2650006, 2026.

[26] C.-H. He, J.-H. He, FRACTAL, FRACTIONAL CALCULUS, AND AI: ADVANCED TOOLS DRIVING INNOVATION IN MECHANICAL ENGINEERING, *Facta Universitatis, Series: Mechanical Engineering,* Vol. 24, No. 1, pp. 001-020, 2026.